

Microstructure, Mechanical Properties, and Sliding Wear Behavior of Oxide-Dispersion-Strengthened FeMnNi Alloy Fabricated by Spark Plasma Sintering



LU YANG, CANCAN ZHAO, WEIWEI ZHU, ZHUO CHENG, PENGBO WEI,
and FUZENG REN

The face-centered-cubic (fcc) CoCrFeMnNi high-entropy alloy suffers from low strength and wear resistance at ambient temperature. Herein, we developed a strategy to overcome the strength/ductility trade-off and simultaneously increase the wear resistance *via* the *in situ* formation of uniformly dispersed Mn₃O₄ nanoparticles in an ultrafine-grained fcc FeMnNi matrix. The obtained equiatomic FeMnNi alloy exhibited a high yield strength of up to 912 MPa and an elongation of 19 pct. Grain boundary and oxide-dispersion-strengthened were found to be the main strengthening mechanisms. Ball-on-disk wear tests showed that the FeMnNi alloy had low wear rates in the order of 10⁻⁴-10⁻⁵ mm³/(N m) upon sliding against an alumina ball, and the wear mechanism changed from abrasive wear to oxidation and fatigue wear at high loads and sliding velocities. The presence of Mn₃O₄ nanoparticles hindered the severe plastic flow of the fcc matrix during sliding. The excellent combination of strength, ductility, and tribological performance of the present alloy renders it as a promising candidate for structural applications.

<https://doi.org/10.1007/s11661-020-05748-7>

© The Minerals, Metals & Materials Society and ASM International 2020

I. INTRODUCTION

THE conventional alloy design concept is generally based on one or two major elements with the addition of a minor amount of alloying elements to achieve the desired properties. In the past 15 years, a novel alloy design strategy with multi-principal elements (MPE) in equiatomic or near-equiatomic concentrations has been developed. These alloys are referred to as high-entropy alloys (HEAs) or multi-principal element alloys (MPEAs).^[1-3] The term 'high entropy' motivates a definition based on the magnitude of configurational

entropy. In ideal solid solutions, the configurational entropy, $\Delta S_{\text{conf}} = -R\sum n_i \ln(n_i)$, where n_i is the atomic fraction of the i th element and R is the gas constant, increases with the number of alloying elements. Based on this definition, the alloys can be divided into low-entropy alloys ($\Delta S_{\text{conf}} < 0.69R$), medium-entropy alloys ($0.69R \leq \Delta S_{\text{conf}} \leq 1.61R$), and HEAs ($\Delta S_{\text{conf}} > 1.61R$).^[3]

Within the family of HEAs, the single-phase face-centered-cubic (fcc) CoCrFeMnNi Cantor alloy has been one of the most extensively investigated alloys owing to its outstanding ductility,^[4] radiation tolerance,^[5] and fracture toughness especially at cryogenic temperatures.^[6] However, this alloy suffers from low strength (usually $< \sim 400$ MPa) at ambient temperature due to its intrinsic fcc structural characteristics.^[4,7-9] Despite the various mechanisms that have been developed to improve the strength of fcc HEAs, overcoming the strength/ductility trade-off of HEAs remains a challenge.

Regarding the sliding wear behavior of Cantor-alloy-based HEAs systems, earlier studies mainly focused on exploring the effects of the addition of different alloying elements,^[10-14] such as Al,^[10] Ti,^[11] Fe,^[12] and V,^[13] on the microstructure, wear performance, and wear mechanism at room temperature (RT) under dry sliding condition. The HEAs were observed to exhibit better wear resistance than conventional wear-resistant alloys with the same level of hardness. Even under

LU YANG, CANCAN ZHAO, ZHUO CHENG, and FUZENG REN are with the Department of Materials Science and Engineering, Southern University of Science and Technology, Shenzhen, Guangdong 518055, China. Contact e-mail: renfz@sustech.edu.cn WEIWEI ZHU is with the Institute of Applied Physics and Materials Engineering, Faculty of Science & Technology, University of Macau, Macau, China and also with the Department of Electromechanical Engineering, Faculty of Science and Technology, University of Macau, Macau, China. PENGBO WEI is with the Department of Materials Science and Engineering, Southern University of Science and Technology and also with the Department of Mechanical and Aerospace Engineering, The Hong Kong University of Science and Technology, Clear Water Bay, Kowloon, Hong Kong, China.

Manuscript submitted October 16, 2019.

Article published online April 19, 2020

lubrication condition, the AlCoCrFeNiCu HEA also exhibited high wear resistance and the wear mechanism showed signs of inhomogeneous polishing oxidation and abrasive wear.^[15] The friction and wear behaviors of HEAs also depend on the sliding conditions, including the applied load, sliding velocity,^[16] and environment.^[17] More recent research efforts have been devoted to the wear behavior of HEAs at elevated temperatures^[18–24] and these works showed that the wear performance and wear mechanism were temperature dependent, transitioning from abrasive wear at RT to oxidative and delamination wear at elevated temperatures. In addition to the work on the fcc HEAs, there have also been several investigations on body-centered-cubic (bcc) HEAs^[25,26] which also show improved wear behavior compared with conventional alloys. However, the majority of these previous investigations focused on the sliding wear behavior of coarse-grained HEAs. The sliding wear behavior of ultrafine-grained MPEAs has been rarely explored and the corresponding wear mechanism remains unknown.

Among the strengthening mechanisms of fcc HEAs, grain refinement and oxide dispersion strengthening are two promising routes to enhance the mechanical properties of fcc alloys.^[27–30] The formation of oxide nanoparticles in the matrix has also been reported to significantly improve the wear resistance of ultrafine-grained alloys.^[31]

In this study, we aimed to develop a strategy to overcome the strength/ductility trade-off of fcc MPEAs *via* the *in situ* formation of uniformly dispersed nanoscale oxides and to further investigate the sliding wear behavior of ultrafine-grained MPEAs. To this end, we selected a ternary equiatomic FeMnNi MPEA as our model system, on the basis of the following factors: (i) Mn is an element with high affinity toward oxygen, which can lead to the *in situ* formation of oxide dispersion-strengthened alloys; (ii) Co was removed from the classical Cantor alloy composition because of its high cost; and (iii) Cr, as a bcc stabilizer and chemically reactive element, was also removed to reduce the complexity of the formed oxides and bcc phase. The ultrafine-grained FeMnNi MPEAs were fabricated using a combination of high-energy ball milling and spark plasma sintering (SPS), and their microstructure, mechanical properties, and especially dry sliding wear behavior were systematically investigated.

II. EXPERIMENTAL PROCEDURES

A. Fabrication of FeMnNi Alloy

Commercially pure Fe, Mn, and Ni powders were mixed in an equiatomic ratio. The powder mixture was subjected to high-energy ball milling with hardened steel balls (ball-to-powder weight ratio = 5:1) using a SPEX 8000D at RT in an argon glove box for 15 hours. Subsequently, the ball-milled powders were consolidated by SPS (SPS-211Lx, Fujidempa Kogyo, Japan) at 1000 °C and 40 MPa for 5 minutes in a vacuum environment of ~ 6 Pa.

B. Mechanical Tests

Dog-bone-shaped specimens for tensile tests with a gauge length of 4 mm, a width of 2 mm, and thickness of 1 mm were cut from the as-sintered cylindrical alloy using electrical discharge machining. Tensile tests were performed on a universal testing machine (CMT5105, MTS, China) at RT using a nominal strain rate of 10^{-4} s^{-1} . A fine black speckle pattern was painted on a white undercoat on the test section to enable monitoring of the deformation during the test using 2D stereo digital image correlation. Three independent tests were performed to confirm the reproducibility of the results. The Vickers hardness of the samples was measured under a load of 300 gf for 10 seconds. At least ten individual indents were performed for each specimen and the average value and standard deviation were recorded.

C. Wear Testing

Dry sliding tests were performed using a ball-on-disk tribometer (Anton-Parr, Austria) at RT ($25 \pm 1 \text{ }^\circ\text{C}$) in air at a relative humidity of 50 pct. Alumina ball with $\Phi = 6 \text{ mm}$ was selected as the counterpart. Prior to the sliding wear tests, the FeMnNi alloy disks were mechanically polished to a surface roughness of $R_a < 20 \text{ nm}$. The sliding wear tests were performed at loads of 2, 5, 7, and 10 N, with the corresponding Hertzian contact stress of approximately 0.90, 1.23, 1.37, and 1.55 GPa, respectively, at a sliding velocity of 0.1 m/s. To study the effect of the sliding velocity on the wear mechanism, we also varied the sliding velocity to 0.05, 0.1, 0.15, and 0.2 m/s at a fixed load of 5 N. All the wear tests were run over a total sliding distance of 1000 m. The wear rate ω was calculated using the volume loss method, with the wear volume quantitatively measured using a 3D optical microscope (ContourGT-K, Bruker, Germany). The wear rate ω was calculated using the following equation:

$$\omega = \frac{V_{\text{loss}}}{L \times P}, \quad [1]$$

where V_{loss} is the wear volume loss (mm^3), L is the sliding distance (m), and P is the applied normal load (N). Three independent tests were run and the average coefficient of friction (CoF) and wear rate were recorded.

D. Phase Identification and Microstructural Characterization

The phases of both ball-milled powders and the sintered bulk alloy were identified using a diffractometer (Smartlab-9 kW, Rigaku, Japan; Cu-K α radiation, $\lambda = 0.154056 \text{ nm}$, 45 kV, 200 mA) in the 2θ range from 30 to 90 deg with a step size of 0.02 deg and speed of 10 °/min. The elemental distribution was examined by energy-dispersive X-ray (EDX) elemental mapping. The grain size of the bulk alloy was determined by electron backscattered diffraction (EBSD; NordlysNano, Oxford Instruments, UK) with the accelerating voltage and step

size of 20 kV and 40 nm, respectively. The microstructure of the as-sintered alloy was also characterized using analytical transmission electron microscopy (TEM; Tecnai F30, FEI), including high-angle annular dark-field scanning transmission electron microscopy (HAADF-STEM), bright-field TEM (BF-TEM), and high-resolution TEM (HRTEM). The morphology of the wear track was investigated using a combination of scanning electron microscopy (SEM; TESCAN MIRA 3, Czech Republic) and 3D optical microscopy. The size, morphology, and chemical composition of wear debris were analyzed using SEM coupled with EDX. The cross-sectional microstructure of the wear track was characterized using secondary electron imaging mode in a focused ion beam system (FIB; Helios NanoLab 600i, FEI), HAADF-STEM, and BF-TEM. For the wear tracks, the directions normal to the sliding surface, along the sliding direction, and perpendicular to the sliding direction in the sliding plane were defined as ND, SD, and TD, respectively. ND-SD cross-sectional TEM samples were prepared using the standard FIB lift-out method. A platinum strip with a thickness of $\sim 1 \mu\text{m}$ was deposited on the wear track before FIB milling for protection against Ga ion beam damage. Statistical analysis of the size and volume fraction of precipitates was performed using ImageJ software (NIH).

III. RESULTS

A. Microstructure Characterization

Figure 1(a) presents the XRD patterns of the Fe, Mn, and Ni starting powder mixture and the ball-milled powders after different times. After 10 hours of ball milling, the individual reflections of Fe, Mn, and Ni completely disappeared, and only a single fcc solid-solution phase was present. No

significant differences were observed in the XRD patterns upon extending the ball milling time to 15 hours. The 15 hours ball-milled powder was then used for SPS. The relative density of the bulk FeMnNi alloy exceeded 97 pct. An XRD pattern of the FeMnNi alloy is presented in Figure 1(b). In addition to the primary fcc reflections, a small amount of manganese oxide (Mn_3O_4) was also present. The lattice parameter of the fcc matrix was determined to be 3.638 Å.

Figure 2(a) presents the backscattered electron (BSE) image and the corresponding EDX elemental maps of the spark-plasma-sintered FeMnNi alloy. The dark contrast in the BSE image indicates the presence of fine Mn_3O_4 nanoparticles. EDX elemental maps confirmed the uniform distribution of Fe, Mn, and Ni. The EBSD inverse pole figure (IPF) map showed the grain size and orientation of the fcc matrix (Figure 2(b)). Figure 2(c) presents the statistical analysis of the grain size distribution of the fcc matrix, ranging from tens of nanometers to $1.5 \mu\text{m}$, with an average grain size of 410 nm. The corresponding EBSD phase map (Figure 2(d)) shows that some Mn_3O_4 nanoparticles were segregated at the grain boundaries of the fcc alloy matrix, with highly homogeneous distributions.

To further evaluate the Mn_3O_4 particles distribution, HAADF-STEM characterization of the FeMnNi alloy was performed, as shown in Figure 3. The HAADF-STEM image reveals that the nanoscale Mn_3O_4 particles were uniformly dispersed in the fcc alloy matrix. Statistical measurements of several HAADF-STEM images (Figure 3(c)) indicated that 64 pct (number fraction) of the Mn_3O_4 particles were located in the grain interior and 36 pct were located at the grain boundaries. The average particle sizes of the intragranular and intergranular oxides (Figure 3(a)) were 38 and 83 nm, respectively. The high-resolution TEM image and the corresponding Fourier transform (FFT) patterns presented in Figure 3(d) show the

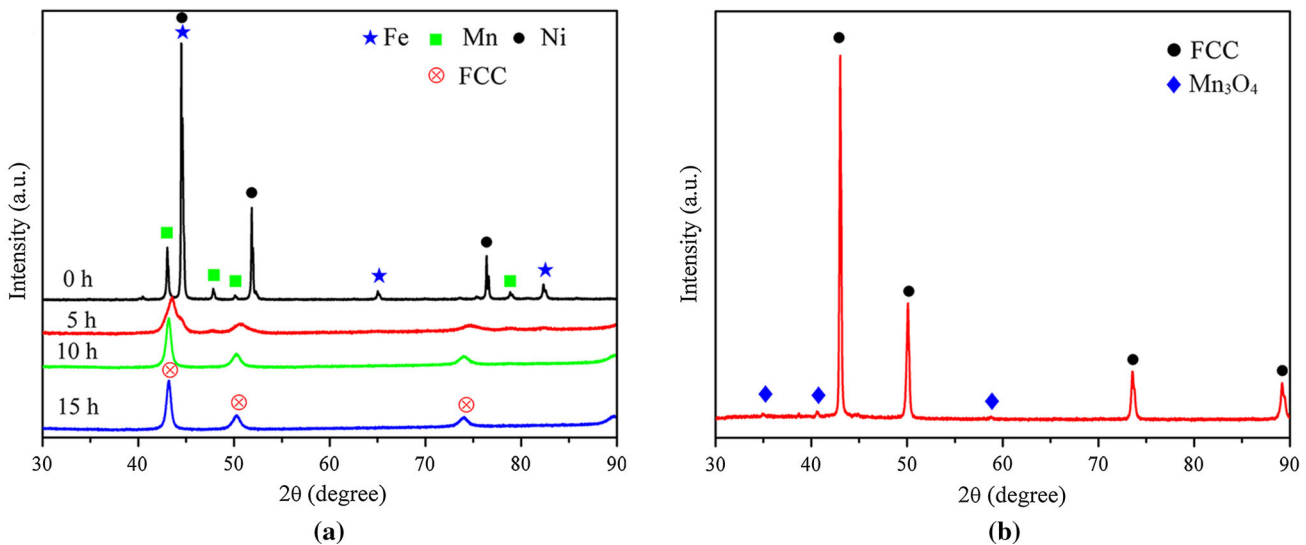


Fig. 1—XRD patterns of the equiatomic Fe, Mn, and Ni powder mixture after ball milling for different times (a) and the as-sintered FeMnNi alloy (b).

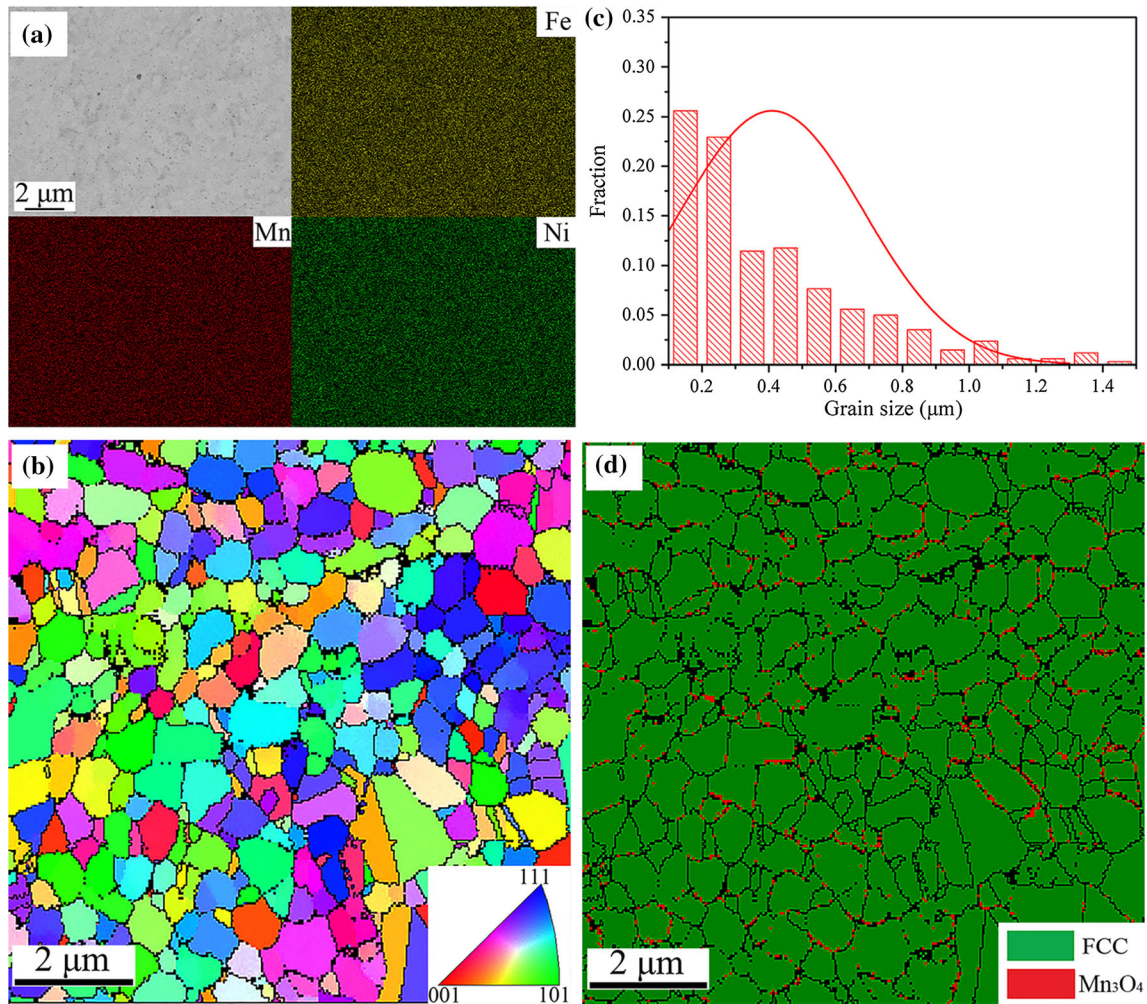


Fig. 2—Composition and grain size of FeMnNi alloy. (a) BSE image with corresponding EDX elemental maps of Fe, Mn, and Ni, (b) EBSD IPF map, (c) grain size distribution of the fcc matrix, and (d) EBSD phase map corresponding to (b).

interface orientation relationship between Mn_3O_4 and the fcc matrix, where $(\bar{1}11)_{\text{Mn}_3\text{O}_4} // (\bar{1}11)_{\text{Matrix}}$ and $[101]_{\text{Mn}_3\text{O}_4} // [101]_{\text{Matrix}}$. The calculated misfit $\delta = 0.82 > 0.25$; thus, the Mn_3O_4 particles and fcc matrix were incoherent.^[32]

B. Mechanical Properties

The average hardness of the bulk FeMnNi alloy was measured to be $342 (\pm 8)$ HV. A typical tensile engineering stress–strain curve of the FeMnNi alloy at RT is presented in Figure 4(a). The bulk specimen exhibited a high yield strength of $912 (\pm 7.5)$ MPa, an appreciable elongation of $19 (\pm 0.9)$ pct, and a Young’s modulus of $195 (\pm 9.5)$ GPa. The fracture surface contained features of dimples, a characteristic of ductile fracture mechanism. A comparison of the strength/ductility with that of other reported Co-free HEAs/MPEAs^[33–44] is presented in Figure 4(b). It is evident that the present FeMnNi alloy exhibits a good combination of high strength/ductility.

C. Wear Properties

1. Effect of load on wear behavior

The variation in CoFs of the FeMnNi alloy as a function of sliding distance at a sliding velocity of 0.1 m/s with varying loads is presented in Figure 5(a). The CoF reached a steady state after a run-in period during the initial stage of wear with a sliding distance of ~ 100 m. At a load of 10 N, the CoF showed a periodic change with the sliding distance. The variations of the CoFs and wear rates as a function of applied load at a sliding speed of 0.1 m/s are shown in Figure 5(b). Upon the application of varying loads, the CoFs showed no apparent change and ranged from 0.74 to 0.83; however, the wear rate showed a monotonic increase with the applied load. From 2 to 5 N, the wear rate slightly increased from 2.138×10^{-5} to 3.406×10^{-5} $\text{mm}^3/\text{N m}$, and from 5 to 10 N, the wear rate almost linearly increased with the load.

For further insight into the evolution of the wear mechanism, we also investigated the effect of applied load on the surface morphology of the wear tracks

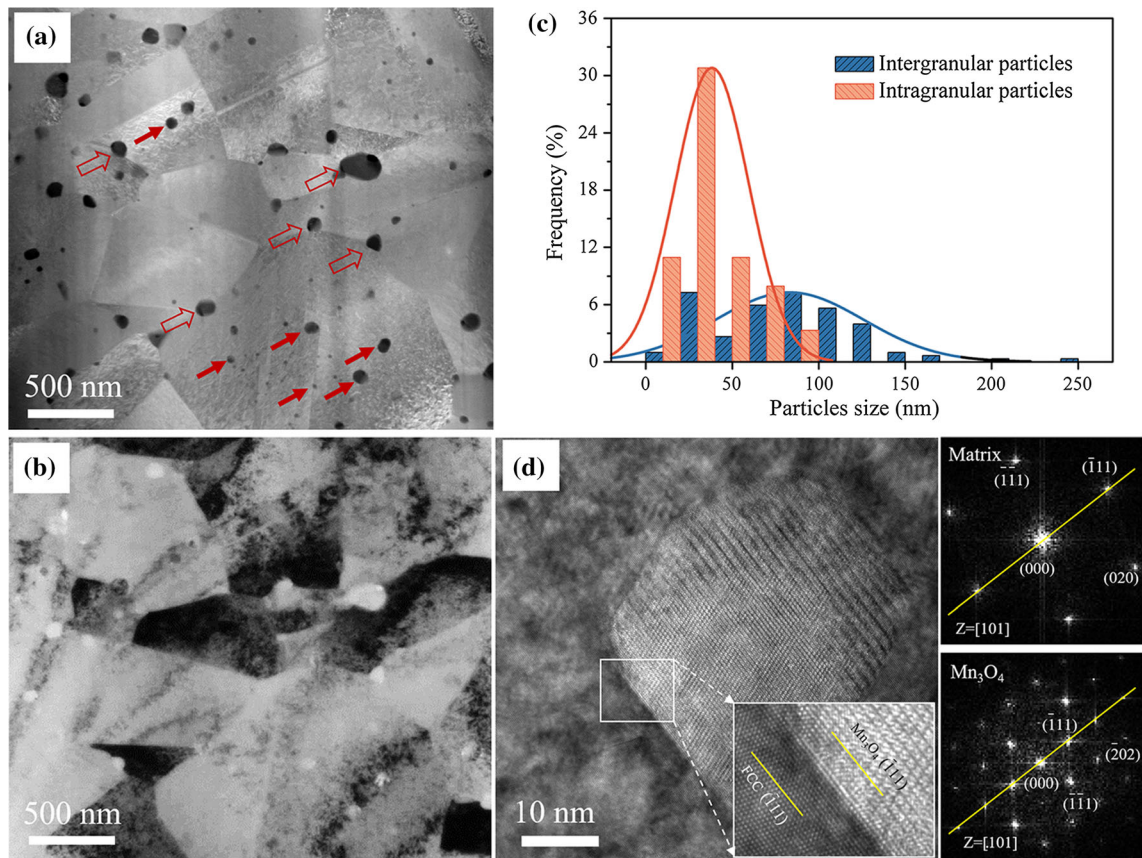


Fig. 3—Microstructure of as-sintered FeMnNi alloy. (a) HAADF-STEM and (b) corresponding BF-TEM images. The intragranular and intergranular Mn_3O_4 particles in (a) are marked by red solid and open arrows, respectively. (c) Particle size distribution of Mn_3O_4 and (d) representative HRTEM image of the interface between the Mn_3O_4 particle and fcc matrix with corresponding FFT patterns (Color figure online).

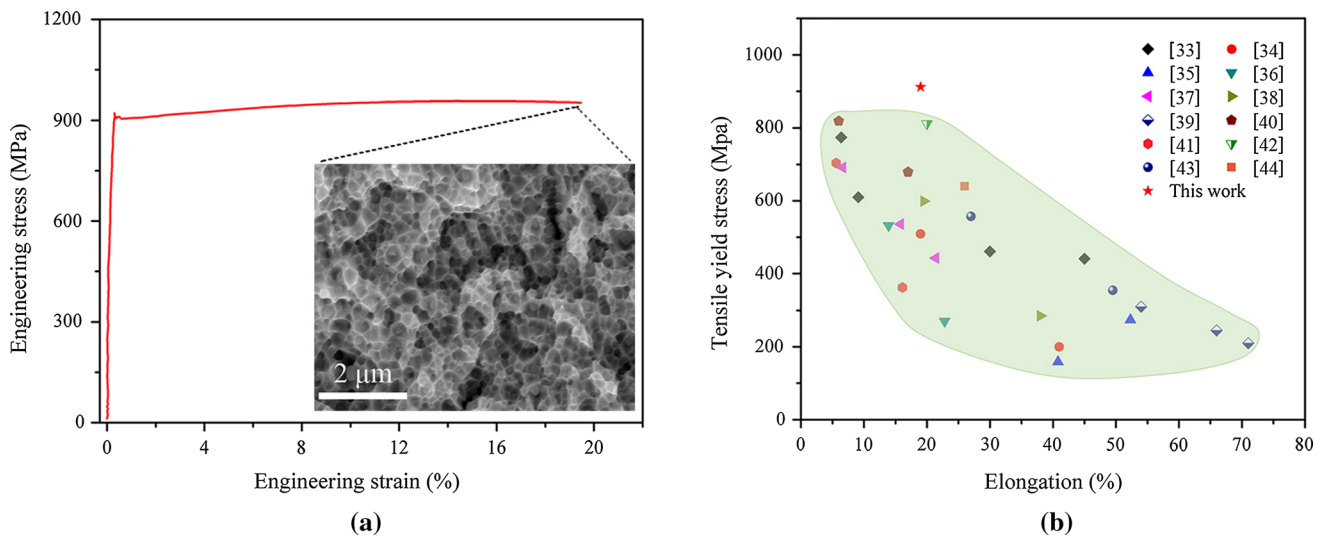


Fig. 4—Mechanical properties of the bulk FeMnNi alloy: (a) Tensile engineering strain–stress curve and fractograph (inset) and (b) comparison of tensile yield strength/elongation to failure combination of the present FeMnNi alloy with other Co-free MPEAs and HEAs in the literatures.^[33–44]

(Figure 6). Distinct differences in the wear surface morphology were observed as a function of the load. At loads of 2, 5, and 7 N, the wear tracks consisted of

shallow and narrow plowing grooves along the SD with a few micro cracks, which are typical characteristics of abrasive wear (Figures 6(a through d)). However, at a

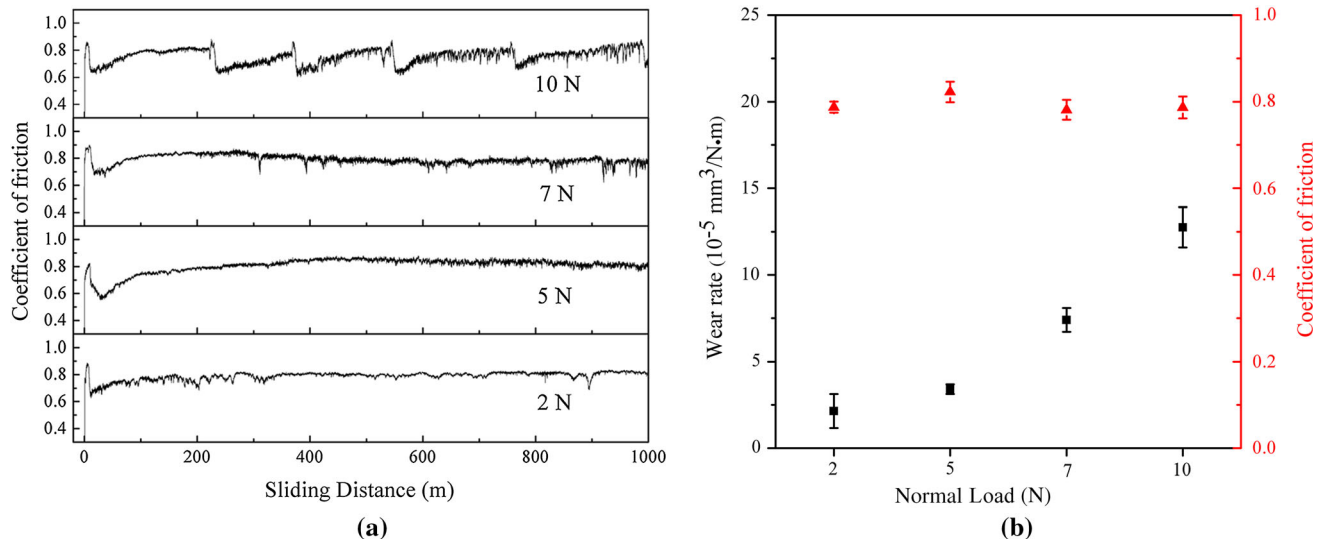


Fig. 5—Effect of applied load on the CoFs and wear rates at a constant sliding velocity of 0.1 m/s: (a) CoFs as a function of sliding distance under varying loads and (b) CoFs and wear rates as a function of applied load.

load of 10 N, craters and oxide layers were present, with a significant reduction in the number of deep grooves compared with those at smaller loads, which are features of oxidation and fatigue wear. The higher-magnification SEM image of the wear track in Figure 6(f) shows that typical fatigue cracks (perpendicular to the SD) were frequently observed within the oxide layers.

The surface profiles of the wear tracks under varying loads at a sliding velocity of 0.1 m/s are presented in Figure 7. The width, maximum depth, and surface roughness showed apparent increases with the applied load during wear. Specifically, at a load of 2 N, the wear track had a width of $435 \mu\text{m}$, maximum depth of $6.9 \mu\text{m}$, and roughness R_a of $0.46 \mu\text{m}$; however, at a load of 10 N, these parameters increase to 1200, 41.3, and $1.86 \mu\text{m}$, respectively.

2. Effect of sliding velocity on wear behavior

The variation in CoFs as a function of sliding velocity for the FeMnNi alloy at a constant load of 5 N is shown in Figure 8(a). Similar to the effect of the applied load, no apparent change in the CoFs was observed with varying sliding velocity; however, the wear rate increased almost linearly with increasing sliding velocity (Figure 8(b)).

The effect of sliding velocity on the surface morphology is shown in Figure 9. At sliding velocities of 0.05 and 0.1 m/s, significant abrasive grooves were observed on the surfaces of the wear tracks along the SD. In contrast, at sliding velocities of 0.15 and 0.2 m/s, many large craters and oxide layers were observed in the wear track. The high-magnification SEM images in Figures 9(d) and (f) further reveal a considerable number of fatigue cracks perpendicular to the SD.

The effect of sliding velocity on the surface profiles of the wear tracks at a constant load of 5 N is shown in Figure 10. From 0.05 to 0.1 m/s, only a slight increase in the width and depth was observed. However, when the sliding velocity was increased to 0.15 m/s, the width and

depth of the wear track significantly increased. The measured roughness R_a after wear increase from 0.63 to $1.25 \mu\text{m}$ upon increasing the sliding velocity from 0.05 to 0.2 m/s (Figures 10(a3 through d3)). These results suggest a transition in the wear mechanism upon changing the sliding velocity from 0.1 to 0.15 m/s.

D. Wear-Induced Subsurface Microstructure

The above results indicate that a similar wear mechanism transition from abrasive wear to oxidation and fatigue wear occurs upon either increasing the load from 7 to 10 N or increasing the sliding velocity from 0.1 to 0.15 m/s. To better understand this wear mechanism transition, we performed detailed characterization of the subsurface microstructure of the alloy upon sliding against an alumina ball under a load of 5 N at sliding velocity of 0.1 and 0.15 m/s. At the sliding velocity of 0.1 m/s, a characteristic plastic deformation zone with a depth of $\sim 2 \mu\text{m}$ was present, where the grains were deformed along the SD owing to wear-induced gradient strain. Upon approaching the sliding surface, the grains were elongated almost in a nanolayered structure parallel to the SD. With increasing depth away from the sliding surface, the grains were gradually recovered to the initial state (Figure 11). To further evaluate the deformed grain structure and the possible material transfer from the counterface alumina ball, we performed further detailed characterization of the microstructure and composition of the severely plastically deformed zone (Figure 11) using analytical TEM. The HAADF-STEM images (Figures 11(b) and (c)) reveal that the Mn_3O_4 nanoparticles at the grain boundaries of the fcc matrix showed no pronounced deformation, despite the severe plastic deformation of the adjacent grains. EDX analysis (Figure 11(d)) revealed a much higher oxygen concentration in the topmost 50 nm below the sliding surface; however, no alumina transfer was detected. The BF-TEM image in

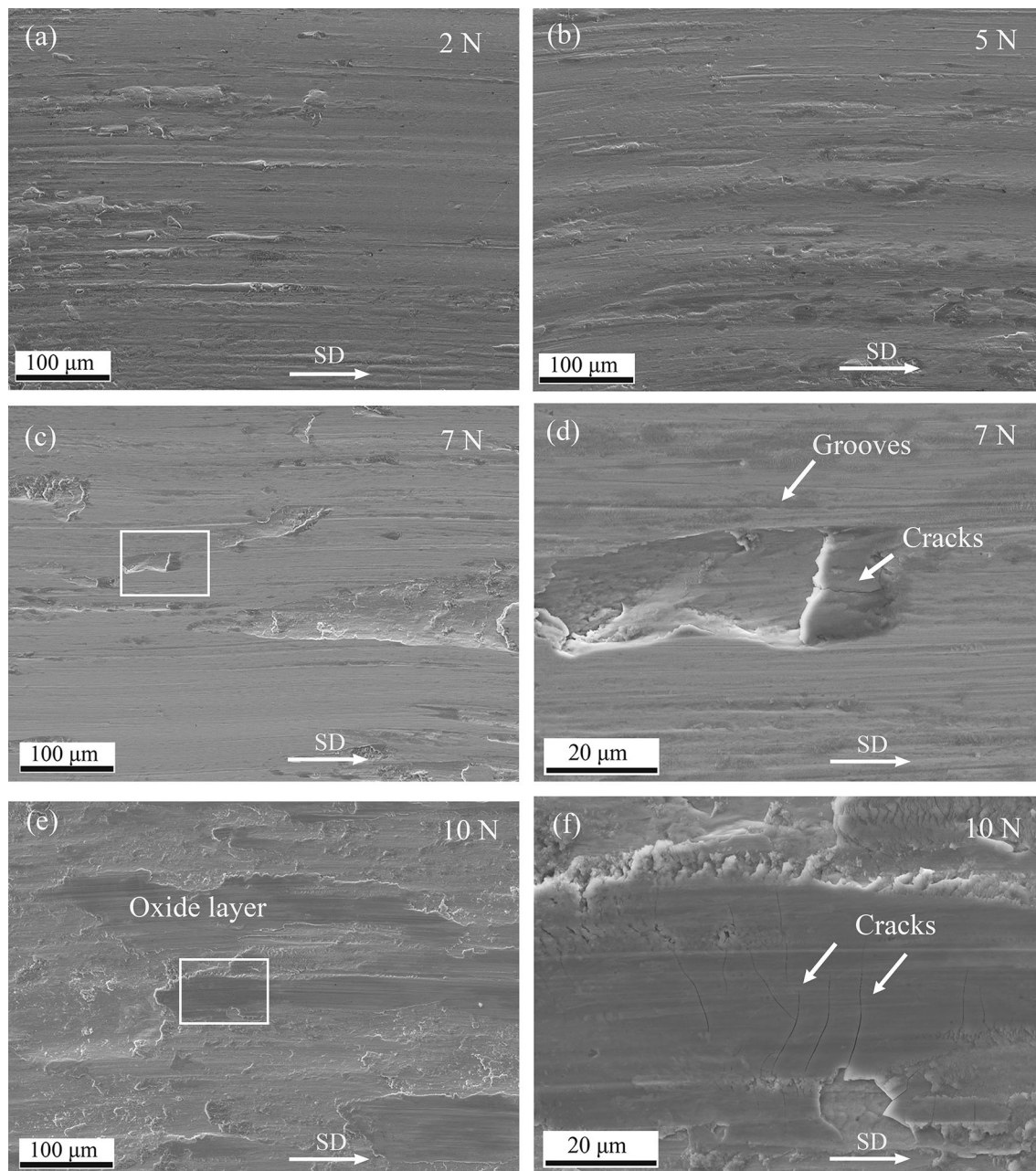


Fig. 6—SEM micrographs of wear tracks of FeMnNi alloy after sliding at a constant sliding velocity of 0.1 m/s under varying loads: (a) 2 N, (b) 5 N, (c, d) 7 N, and (e, f) 10 N. SD denotes the sliding direction.

Figure 11(e) reveals high density of dislocations inside the deformed elongated grains. SAED pattern confirmed that the phase of this zone was predominantly the fcc FeMnNi alloy matrix with a weak shear texture.

A completely different wear-induced subsurface structure was observed at a sliding velocity of 0.15 m/s at the same load of 5 N. Cross-sectional TEM analyses revealed that the worn microstructure consisted of three characteristic regions (Figures 12(a) and (b)). In the topmost $\sim 1.2 \mu\text{m}$, a glaze layer was formed, consisting of equiaxed MnNi_2O_4 and MnFe_2O_4 oxides (Figure 13) with a size of only several nanometers (Figure 13(c)). These oxides originated

from the FeMnNi alloy without the presence of the transferred alumina from the counterface ball. Below the glaze layer was a $2 \mu\text{m}$ -thick nanocrystalline layer, consisting of slightly elongated nanograins with an average thickness of 32 nm. Beyond the nanocrystalline layer was a nanolaminated layer, where the extended layer boundaries were flat and parallel to SD. Low-density isolated dislocations and interconnecting dislocation boundaries were observed. The spacing of the laminated boundaries ranged from 25 to 65 nm with an average thickness of 35 nm. The SAED pattern obtained from these nanolaminates contained elongated spots, indicating small misorientations.

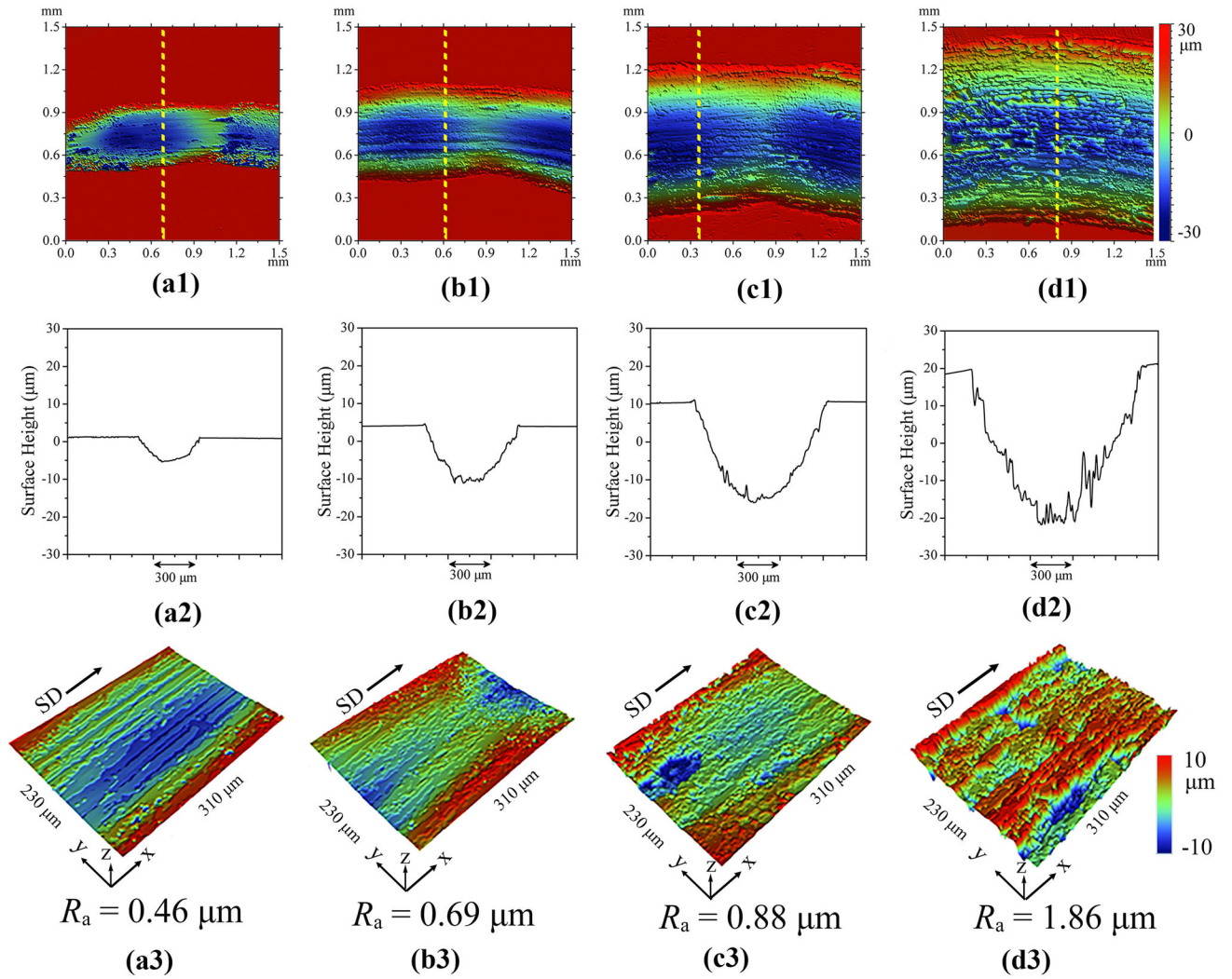


Fig. 7—Surface profiles of the wear tracks after sliding under varying loads at a constant sliding velocity of 0.1 m/s: (a1 through a3) 2 N, (b1 through b3) 5 N, (c1 through c3) 7 N, and (d1 through d3) 10 N. From top to bottom, the three rows present false-color surface height images, 2D cross-sectional profiles, and 3D surface profile images.

IV. DISCUSSION

A. Strengthening Mechanisms

One important finding of this study is that the present FeMnNi alloy fabricated by high-energy ball milling and SPS exhibited a combination of high yield strength (of 912 MPa) and ductility (elongation of 19 pct). This good combination of high strength-ductility can be attributed to the microstructure of the alloy consisting of an ultrafine-grained fcc matrix with a high content of uniformly dispersed Mn_3O_4 nanoparticles. The strengthening mechanisms in the FeMnNi alloy are now analyzed, and the respective quantitative contribution of each strengthening mechanism is estimated. Grain boundary (GB) strengthening ($\Delta\sigma_{\text{GB}}$), dislocation strengthening ($\Delta\sigma_{\text{Dis}}$), and oxide dispersion

strengthening ($\Delta\sigma_{\text{O}}$) are considered the main strengthening mechanisms in the FeMnNi alloy. The yield strength can be calculated by summing up the individual contribution from each strengthening mechanism:

$$\sigma_y = \sigma_0 + \Delta\sigma_{\text{GB}} + \Delta\sigma_{\text{O}} + \Delta\sigma_{\text{Dis}}, \quad [2]$$

where σ_0 is 119 MPa, the lattice friction stress of the FeMnNi matrix.^[45] The contribution of solid-solution strengthening ($\Delta\sigma_{\text{ss}}$) is not considered here because of the relatively small atomic size difference of the elements in the solid-solution phase.

1. GB strengthening

For the grain size level of the present FeMnNi alloy, GB strengthening conforms to the Hall-Petch relationship^[46]:

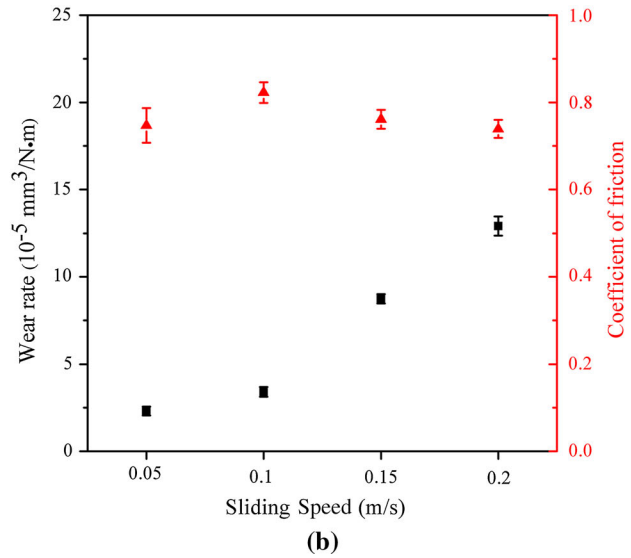
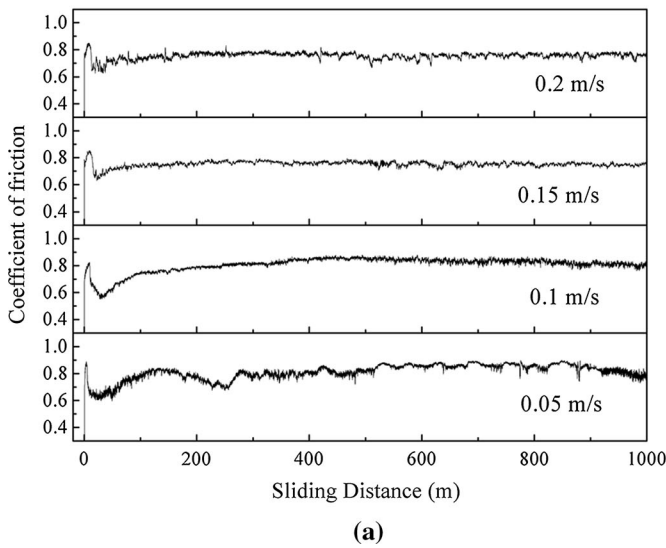


Fig. 8—Effect of sliding velocity on CoFs and wear rates under a constant load of 5 N: (a) CoFs as a function of sliding distance at different sliding velocities and (b) CoFs and wear rates as a function of sliding velocity.

$$\Delta\sigma_{GB} = K^{HP} d^{-1/2}, \quad [3]$$

where K^{HP} is the Hall-Petch coefficient with a value of $381 \text{ MPa } \mu\text{m}^{1/2}$ [45] and d is the average grain size (410 nm). Consequently, $\Delta\sigma_{GB}$ is calculated to be 595 MPa.

2. Oxide dispersion strengthening

The contribution of oxide dispersion strengthening ($\Delta\sigma_O$) can be calculated using the following equation[47]:

$$\Delta\sigma_O = \Delta\sigma_{intra} + \Delta\sigma_{inter}, \quad [4]$$

where $\Delta\sigma_{intra}$ and $\Delta\sigma_{inter}$ are the strength increases caused by intragranular and intergranular particles, respectively. The intragranular particles serve as obstacles to moving dislocations in the grain interior, and $\Delta\sigma_{intra}$ is usually given by the following equation[47]:

$$\Delta\sigma_{intra} = \varphi \frac{Gb}{\lambda_{intra}} = \frac{\varphi Gb}{d_{intra}} \left(\frac{6f_{intra}}{\pi} \right)^{1/3} \quad [5]$$

where φ is a constant in the order of 2.[47] $G = 73 \text{ GPa}$ is the shear modulus of the FeMnNi matrix,[7] b is the Burgers vector ($b = \frac{\sqrt{2}}{2}a$, a is the lattice parameter) of the fcc matrix (0.257 nm), d_{intra} is the intragranular particle size (38 nm), λ_{intra} is the inter-particle spacing, and f_{intra} is the volume fraction of intragranular particles (0.9 pct). Therefore, $\Delta\sigma_{intra}$ is calculated to be $\sim 255 \text{ MPa}$.

For the intergranular particles, the load-bearing strength increase was calculated using a simple model for a particulate-reinforced metal matrix composite[47,48]:

$$\Delta\sigma_{inter} = 0.5f_{inter}\sigma_m, \quad [6]$$

where f_{inter} is the volume fraction of the intergranular oxide particles (2.1 pct) and σ_m is the yield strength of the matrix which is equal to the sum of the first two terms in Eq. [2]. The estimated incremental contribution from intergranular particles, $\Delta\sigma_{inter}$, is only $\sim 5 \text{ MPa}$. Therefore, the calculated value of $\Delta\sigma_O$ is $\sim 260 \text{ MPa}$.

3. Dislocation strengthening

In general, a higher dislocation density leads to a higher yield strength. The increase of yield strength due to dislocation strengthening can be calculated using the following equation[49]:

$$\Delta\sigma_{Dis} = M\alpha Gb\rho^{1/2}, \quad [7]$$

where α is 0.2 for fcc metals, ρ represents the dislocation density, and b is the burger vector. The dislocation density ρ is calculated using the following equation[50]:

$$\rho = \frac{2\sqrt{3}\varepsilon}{db}, \quad [8]$$

where d , ε , and b are the grain size (410 nm), microstrain, and Burgers vector, respectively. ε was estimated using the Williamson-Hall method,[51] and the true XRD peak broadening B consists of both crystallite size broadening and strain broadening, as shown in the equation[52]:

$$B \cos \theta_B = \frac{K\lambda}{d} + 4\varepsilon \sin \theta_B \quad [9]$$

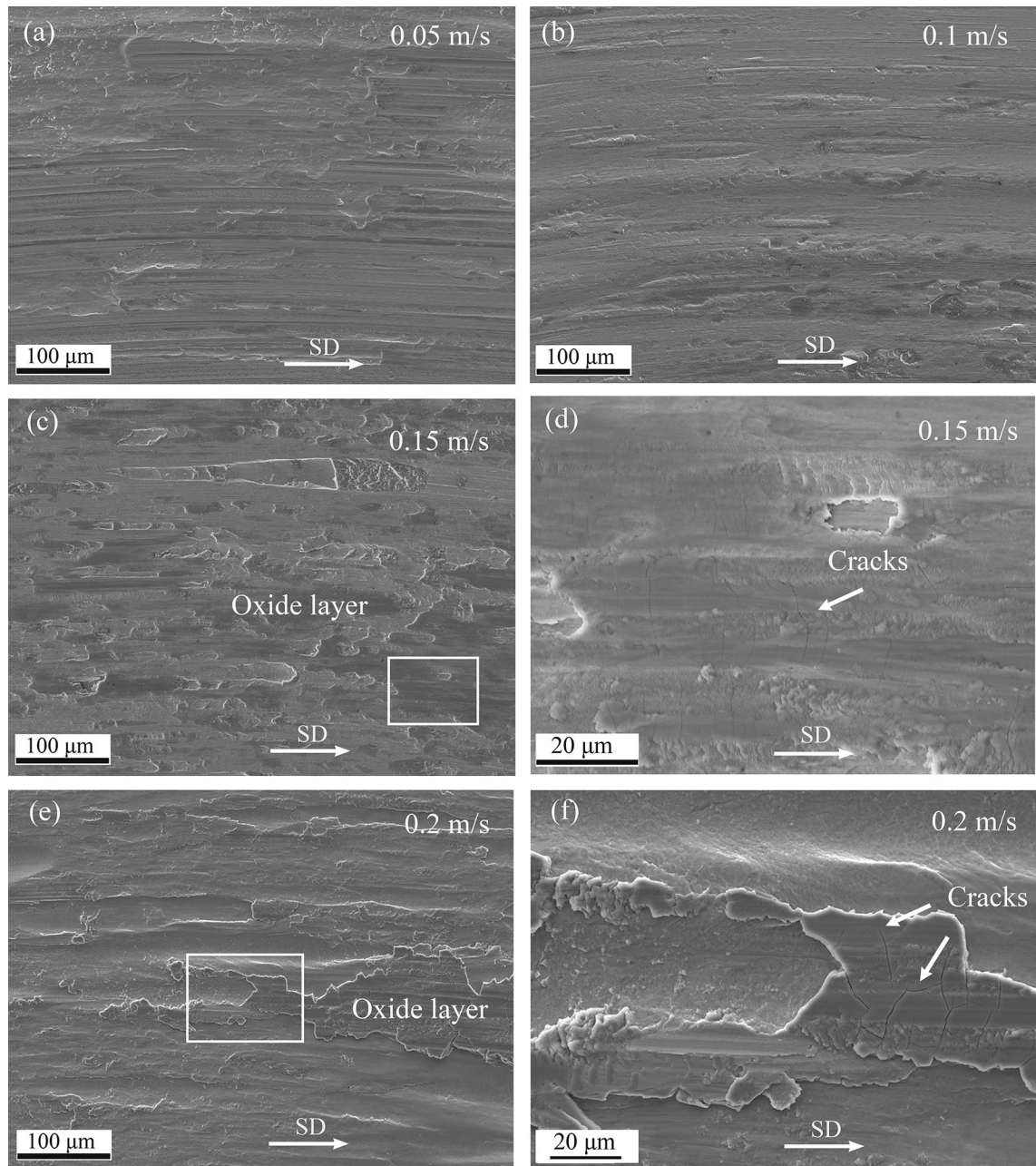


Fig. 9—SEM micrographs of wear tracks of FeMnNi alloy after sliding at different sliding velocities under a constant load of 5 N: (a) 0.05, (b) 0.1, (c, d) 0.15, and (e, f) 0.2 m/s.

Here, λ is the wavelength of Cu $K\alpha$ radiation (0.15406 nm), K is a constant (0.9), and θ_B is the Bragg angle. The slope of the linear fit of the $B\cos\theta_B-4\sin\theta_B$ plot was used to determine the value of $\varepsilon = 0.086$, and combining Eqs. [8] and [9], the dislocation density for the FeMnNi alloy was calculated to be $1.43 \times 10^{13} \text{ m}^{-2}$. Inputting this value into Eq. [7], the yield strength

increase from dislocation strengthening ($\Delta\sigma_{\text{Dis}}$) is estimated to be 43 MPa.

Based on the discussion above, the overall yield strength was calculated to be $\sigma_y = 1017 \text{ MPa}$, which agrees reasonably well with the experimental yield strength of 912 MPa. The overestimation of the yield strength may arise from the fact that the Mn_3O_4

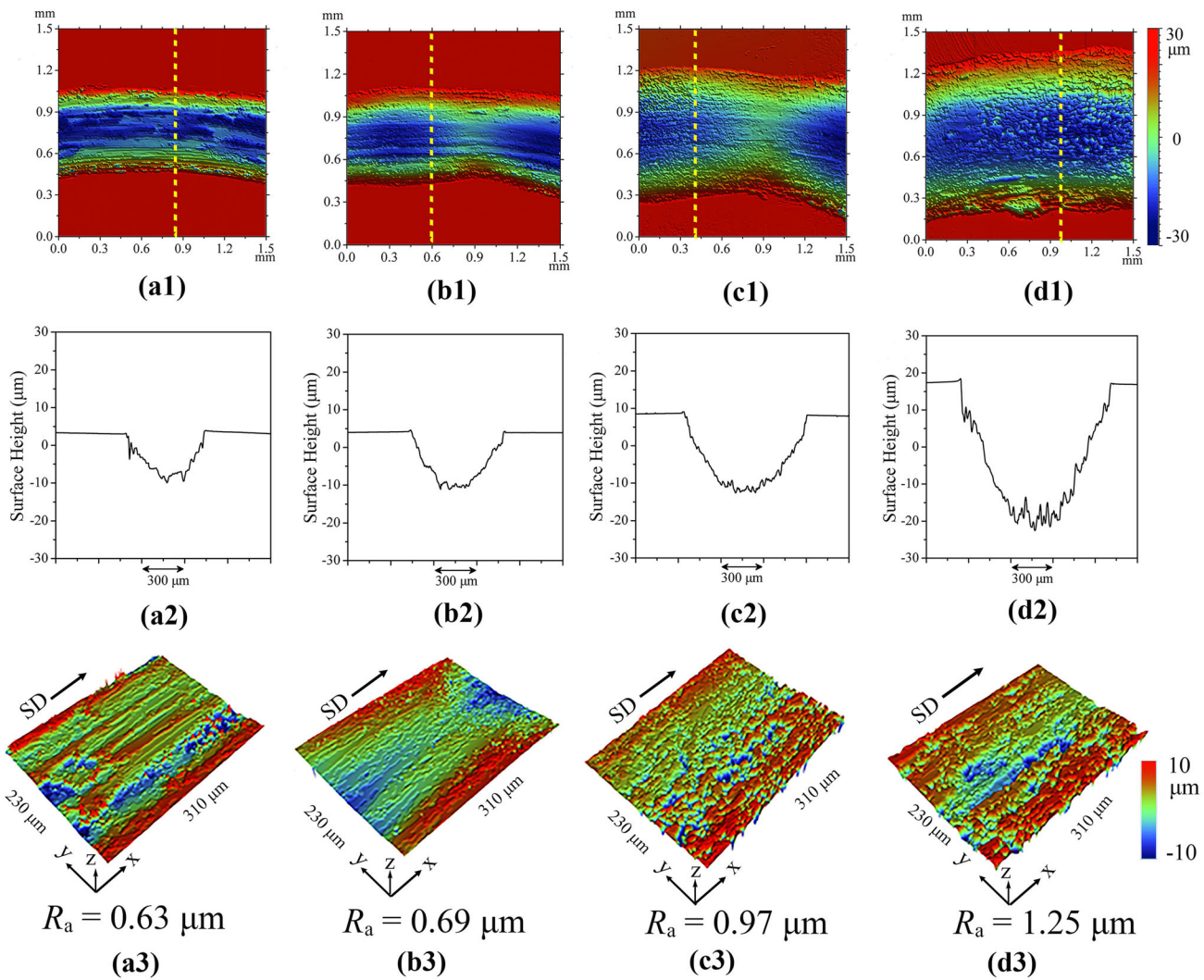


Fig. 10—Surface profiles of wear tracks after sliding at different sliding velocities under a constant load of 5 N: (a1 through a3) 0.05, (b1 through b3) 0.1, (c1 through c3) 0.15, and (d1 through d3) 0.2 m/s. From top to bottom, the three rows present false-color surface height images, 2D cross-sectional profiles, and 3D surface profile images.

particles were treated as spherical in the calculation of precipitation strengthening. However, many of the particles are actually irregular plate-shaped particles, which are expected to produce more resistance to dislocation motion than spherical particles.^[52]

The above quantitative analysis demonstrates that the high yield strength of the UFG FeMnNi alloy can primarily be attributed to grain boundary and oxide dispersion strengthening.

B. Wear Mechanisms

The worn surface morphology and subsurface microstructure reveal that both the applied load and sliding velocity affect the wear mechanism. The

transition of the wear mechanism from abrasive wear to oxidative and fatigue wear was observed either at a load of 10 N or at a sliding velocity of 0.15 m/s. The effects of load and sliding velocity on the wear mechanism transition are usually attributed to the effect of shear stress and strain rate on the plastic deformation. The wear transitions are caused by the external stress and strain rate exceeding the threshold value of the material and causing intergranular fracture.^[53] Larger loads and sliding velocities result in the wear transition occurring earlier.^[54] In addition, for the same duration, a greater load or sliding velocity will result in more severe wear (Figures 7 and 9). A higher load and sliding velocity may also lead to an increase in frictional heat, which will result in a temperature rise at the contact

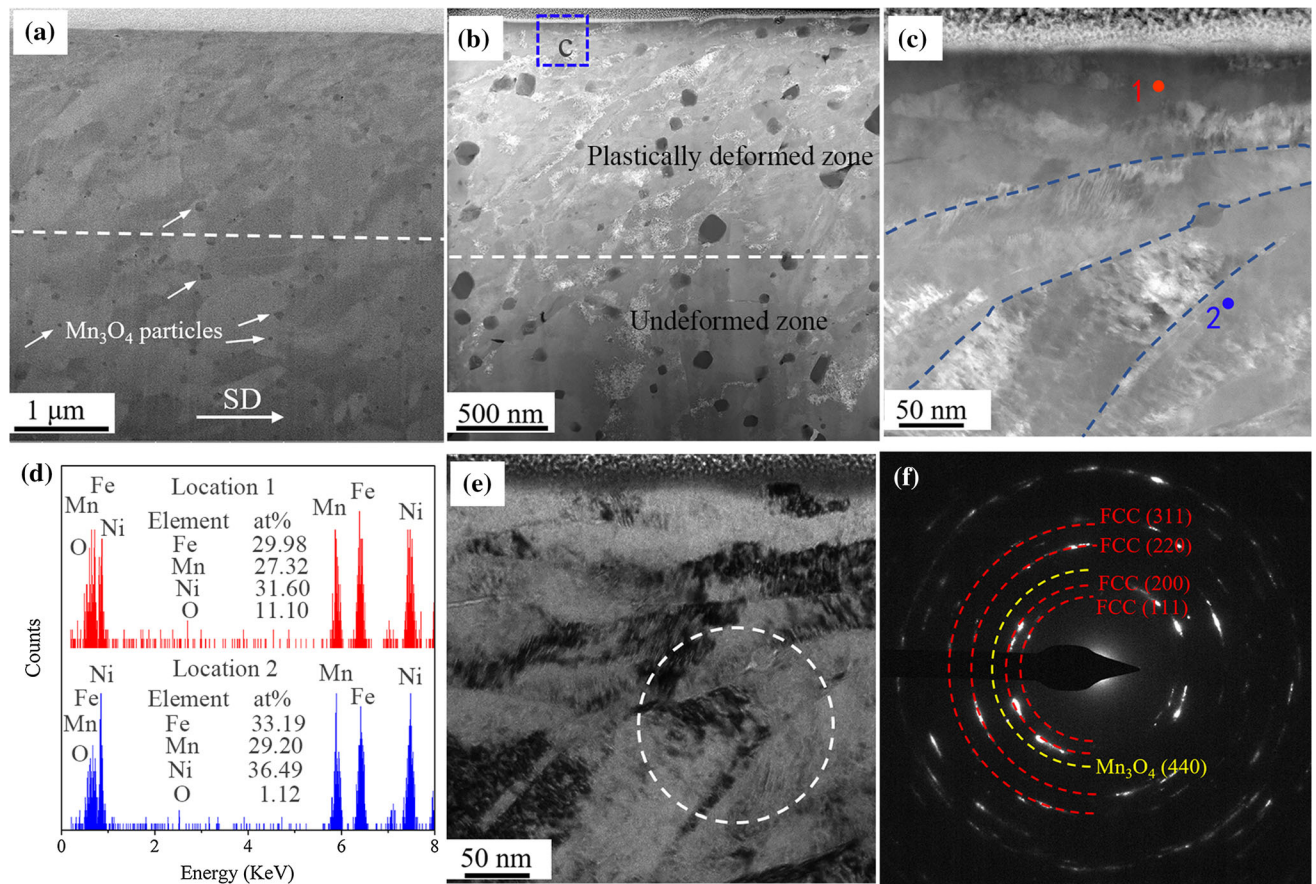


Fig. 11—ND-SD cross-sectional subsurface microstructure of FeMnNi alloys after sliding against alumina ball with a load of 5 N and sliding velocity of 0.1 m/s: (a) FIB-milled secondary electron image, (b) HAADF-STEM image, (c) high-magnification HAADF-STEM image of the selected topmost region in (b), (d) EDX spectra of the two locations in (c), (e) BF-TEM image corresponding to (c), and (f) SAED pattern of (e).

interface and thereby resulting in higher surface roughness and an accelerated oxidation process.^[54,55] Moreover, the rise in surface temperature may also result in thermal softening of the alloy, leading to reduction of the hardness and fracture toughness.^[53,54]

At a smaller load or sliding velocity, the wear-imposed strain/strain rate below the sliding surface is relatively small, leading to a relatively low degree of plastic deformation. In addition, the generated frictional heat is insufficient to cause severe oxidation of the surface material. During sliding, the dispersed hard Mn_3O_4 nanoparticles can serve as obstacles that impede grain boundary motion in the matrix and further hinder severe plastic flow of the matrix, leading to a small deformation depth. At a higher load or sliding velocity, large strains/strain rates facilitate dislocation multiplication and the pile-up of the dislocations. The formation of low-angle GBs in the form of nanoscale-laminated structures is energetically

favoured.^[56] To accommodate large plastic strains, friction shear induces geometrically necessary dislocation boundaries (GNBs) and short incidental dislocation boundaries (IDBs) into the formation of a nanolaminated structure.^[56] Large strains/strain rates can also lead to further refinement of the nanolaminated structure with the formation of equiaxed nano-grains resulting from dislocation accumulation and sub-boundary development.^[57] Repeated stress and the frictional heat near the surface can induce the formation of oxides, detach the material, generate particles, and then cold weld them onto the surface again, eventually leading to the formation of a nanostructured glaze layer (Figure 13). The formed brittle glaze layer may facilitate crack propagation (Figure 12(b)) and result in higher surface roughness and wear rate. Therefore, the wear mechanism is dominated by oxidation and fatigue wear at higher load and sliding velocity.

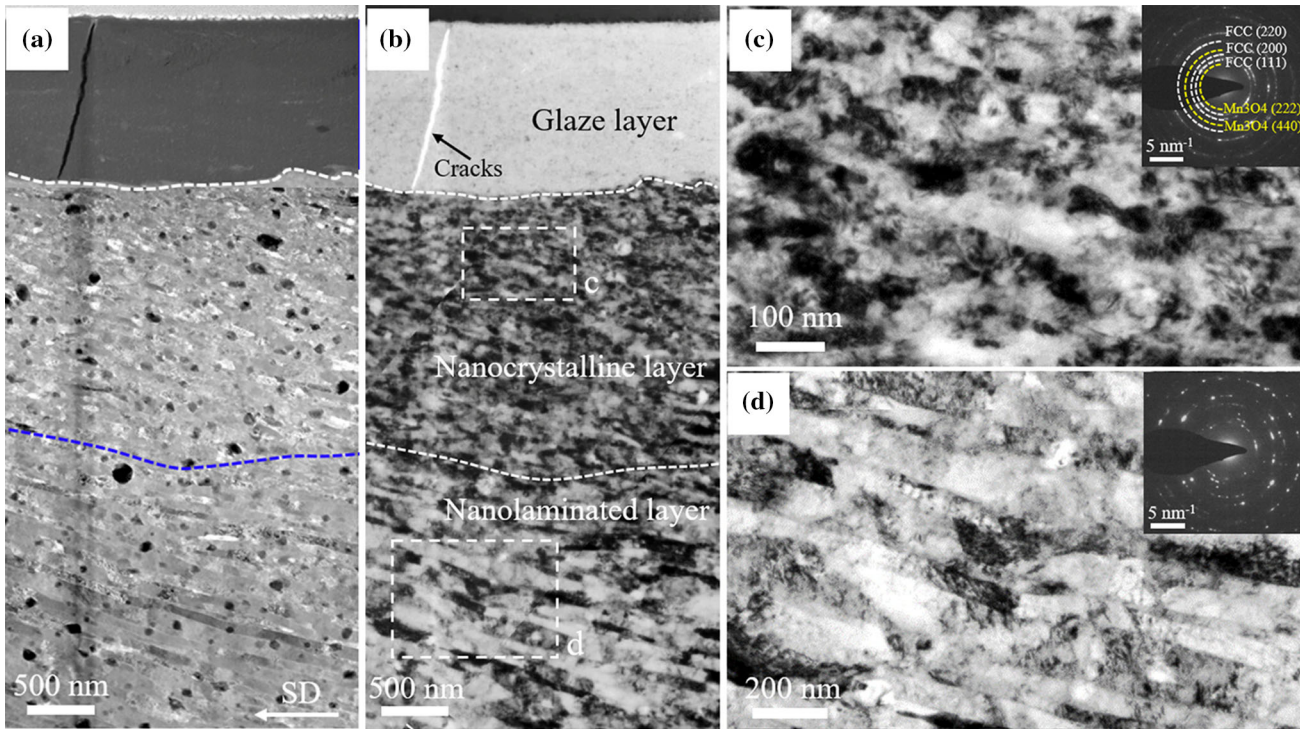


Fig. 12—ND-SD cross-sectional subsurface microstructure of FeMnNi alloy after sliding against alumina ball with a load of 5 N and sliding velocity of 0.15 m/s: (a) HAADF-STEM image, (b) corresponding bright-field TEM image, (c) and (d) high-magnification bright-field TEM images with corresponding SAED patterns (insets) of the selected two areas at different depths away from the sliding surface in (b), respectively.

V. CONCLUSIONS

In this work, an ultrafine-grained FeMnNi alloy was fabricated using a combination of high-energy ball milling and SPS. We systematically investigated its mechanical properties and sliding wear behavior through detailed characterization of the microstructure. The following conclusions can be drawn:

1. The microstructure of the fabricated FeMnNi alloy consisted of an fcc matrix with an average grain size of 410 nm and 3.0 vol pct nanoscale Mn_3O_4 particles.
2. The FeMnNi alloy exhibited a good combination of yield strength (912 MPa) and elongation (19 pct). GB strengthening and oxide dispersion strengthening were the main strengthening mechanisms.
3. The wear rate increased with increasing applied load and sliding velocity, and the wear mechanism changed from abrasive wear to oxidation and fatigue wear at high load or sliding velocity.
4. Distinct subsurface gradient microstructures were formed below the sliding surface, depending on the applied load and sliding velocity. At a low load and sliding velocity, a relatively low degree of plastic deformation was observed below the sliding surface; however, high load and sliding velocity induced the formation of a gradient microstructure consisting of a nanostructured glaze layer, nanocrystalline layer, and nanolaminated layer.

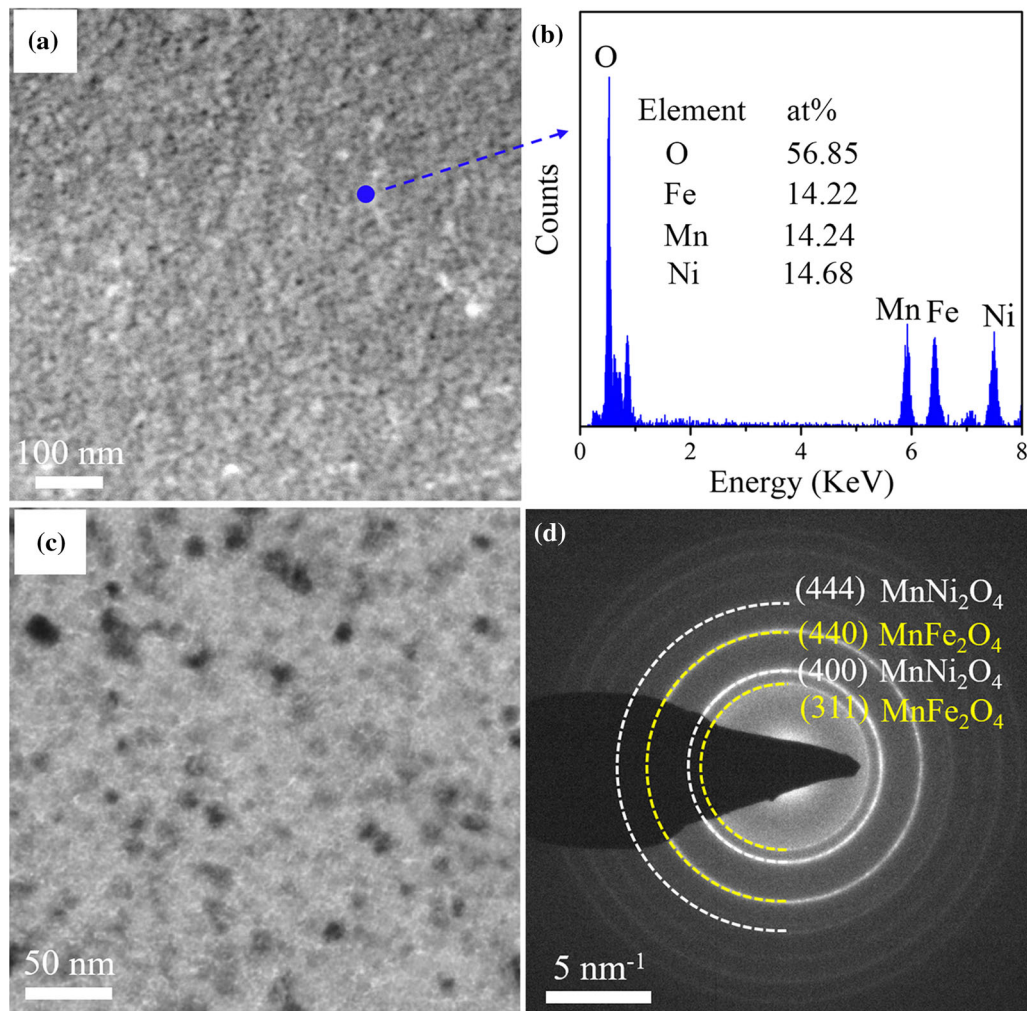


Fig. 13—Microstructure and composition of glaze layer formed on FeMnNi alloy after sliding against alumina ball with a load of 5 N and a sliding velocity of 0.15 m/s: (a) HAADF-STEM image, (b) typical EDX spectrum, (c) bright-field TEM image, and (d) SAED pattern of (c).

ACKNOWLEDGMENTS

This work was financially supported by the Fundamental Research Program of Shenzhen (Grant No. JCYJ20170412153039309) and Guangdong Innovative & Entrepreneurial Research Team Program (No. 2016ZT06C279). This work was also supported by the Pico Center at SUSTech that receives support from the Presidential Fund and Development and Reform Commission of Shenzhen Municipality. The authors would also like to thank Tiffany Jain, M.S., from Liwen Bianji, Edanz Group China (www.liwenbianji.cn/ac), for editing the English text of a draft of this manuscript.

REFERENCES

- J.W. Yeh, S.K. Chen, S.J. Lin, J.Y. Gan, T.S. Chin, T.T. Shun, C.H. Tsau, and S.Y. Chang: *Adv. Eng. Mater.*, 2004, vol. 6 (5), pp. 299–303.
- B. Cantor, I.T.H. Chang, P. Knight, and A.J.B. Vincent: *Mater. Sci. Eng., A*, 2004, vols. 375–377, pp. 213–18.
- D.B. Miracle and O.N. Senkov: *Acta Mater.*, 2017, vol. 122, pp. 448–511.
- F. Otto, A. Dlouhy, Ch. Somsen, H. Bei, G. Eggeler, and E.P. George: *Acta Mater.*, 2013, vol. 61, pp. 5743–55.
- C. Lu, L. Niu, N. Chen, K. Jin, T. Yang, P. Xiu, Y. Zhang, F. Gao, H. Bei, S. Shi, M.R. He, I.M. Robertson, W.J. Weber, and L. Wang: *Nat. Commun.*, 2016, vol. 7, p. 13564.
- B. Gludovatz, A. Hohenwarter, D. Catoor, E.H. Chang, E.P. George, and R.O. Ritchie: *Science*, 2014, vol. 345, pp. 1153–58.
- Z. Wu, H. Bei, G.M. Pharr, and E.P. George: *Acta Mater.*, 2014, vol. 81, pp. 428–41.
- M.J. Yao, K.G. Pradeep, C.C. Tasan, and D. Raabe: *Scripta Mater.*, 2014, vols. 72–73, pp. 5–8.
- Y.F. Ye, Q. Wang, J. Lu, C.T. Liu, and Y. Yang: *Mater. Today*, 2016, vol. 19, pp. 349–62.
- J.M. Wu, S.J. Lin, J.W. Yeh, S.K. Chen, and Y.S. Huang: *HC ChenWear*, 2006, vol. 59, pp. 6308–17.
- M.H. Chuang, M.H. Tsai, W.R. Wang, S.J. Lin, and J.W. Yeh: *Acta Mater.*, 2011, vol. 59, pp. 6308–17.
- C.Y. Hsua, T.S. Sheu, J.W. Yeh, and S.K. Chen: *Wear*, 2010, vol. 268, pp. 653–59.
- M.R. Chen, S.J. Lin, J.W. Yeh, S.K. Chen, Y.S. Huang, and M.H. Chuang: *Metall. Mater. Tran. A*, 2006, vol. 37A, pp. 1363–69.
- C.Y. Hsu, J.W. Yeh, S.K. Chen, and T.T. Shun: *Metall. Mater. Tran. A*, 2004, vol. 35A, pp. 1465–69.
- H. Duan, Y. Wu, M. Hua, C. Yuan, D. Wang, J. Tu, H. Kou, and J. Li: *Wear*, 2013, vol. 297, pp. 1045–51.

16. G. Deng, A.K. Tieu, X. Lan, L. Su, L. Wang, Q. Zhu, and H. Zhu: *Tribol. Int.*, 2020, vol. 144, p. 106116.
17. Y. Liu, S. Ma, M.C. Gao, C. Zhang, T. Zhang, H. Yang, Z. Wang, and J. Qiao: *Metall. Mater. Tran. A*, 2016, vol. 47A, pp. 3312–21.
18. A. Verma, P. Tarate, A.C. Abhyankar, M.R. Mohape, D.S. Gowtam, V.P. Deshmukh, and T. Shanmugasundaram: *Scripta Mater.*, 2019, vol. 161, pp. 28–31.
19. J. Joseph, N. Haghdad, K. Shamlaye, P. Hodgson, M. Barnett, and D. Fabijanic: *Wear*, 2019, vols. 428–429, pp. 32–44.
20. Y. Yu, F. He, Z. Qiao, Z. Wang, W. Liu, and J. Yang: *J. Alloys Compd.*, 2019, vol. 775, pp. 1376–85.
21. M. Chen, L. Lan, X. Shi, H. Yang, M. Zhang, and J. Qiao: *J. Alloy Compd.*, 2019, vol. 777, pp. 180–89.
22. L.M. Du, L.W. Lan, S. Zhu, H.J. Yang, X.H. Shi, P.K. Liaw, and J.W. Qiao: *J. Mater. Sci. Technol.*, 2019, vol. 35, pp. 917–25.
23. M. Löbel, T. Lindner, R. Pippig, and T. Lampke: *Entropy*, 2019, vol. 21.
24. S. Alvi and F. Akhtar: *Wear*, 2019, vols. 426–427, pp. 412–19.
25. Y.X. Ye, C.Z. Liu, H. Wang, and T.G. Nieh: *Acta Mater.*, 2018, vol. 147, pp. 78–89.
26. A. Poulia, E. Georgatis, A. Lekatou, and A. Karantzalis: *Adv. Eng. Mater.*, 2017, vol. 19, p. 1600535.
27. S.H. Joo, H. Kato, M.J. Jang, J. Moon, E.B. Kim, S.J. Hong, and H.S. Kim: *J. Alloy Compd.*, 2017, vol. 698, pp. 591–604.
28. N. Oono, Q.X. Tang, and S. Ukai: *Mater. Sci. Eng. A*, 2016, vol. 649, pp. 250–53.
29. H. Hadrabaa, Z. Chlupa, A. Dlouhaya, F. Dobesa, P. Roupcovaa, M. Vilemovab, and J. Matejicekb: *Mater. Sci. Eng. A*, 2017, vol. 689, pp. 252–56.
30. X. Liu, H. Yin, and Y. Xu: *Materials*, 2017, vol. 10, pp. 1312–32.
31. G. Purcek, O. Saray, F. Rubitschek, T. Niendorf, H.J. Maier, and I. Karaman: *Acta Mater.*, 2011, vol. 59, pp. 7683–94.
32. J. Ribis and Y.D. Carlan: *Acta Mater.*, 2012, vol. 60, pp. 238–52.
33. X. Jin, J. Bi, L. Zhang, Y. Zhou, X. Du, Y. Liang, and B. Li: *J. Alloy Compd.*, 2019, vol. 770, pp. 655–61.
34. Z. Wang, A. Genc, and I. Baker: *Mater. Charact.*, 2017, vol. 132, pp. 156–61.
35. Z. Wang, I. Baker, Z. Cai, S. Chen, J.D. Poplawsky, and W. Guo: *Acta Mater.*, 2016, vol. 120, pp. 228–39.
36. Z. Wang, M. Wu, Z. Cai, S. Chen, and I. Baker: *Intermetallics*, 2016, vol. 75, pp. 79–87.
37. M. Wu, P.R. Munroe, and I. Baker: *J. Mater. Sci.*, 2016, vol. 51, pp. 7831–42.
38. I. Baker, F. Meng, M. Wu, and A. Brandenberg: *J. Alloy. Compd.*, 2016, vol. 656, pp. 458–64.
39. N.D. Stepanov, D.G. Shaysultanov, M.A. Tikhonovsky, and G.A. Salishchev: *Mater. Des.*, 2015, vol. 87, pp. 60–65.
40. F. Meng, J. Qiu, and I. Baker: *Mater. Sci. Eng. A*, 2013, vol. 586, pp. 45–52.
41. C. Ng, S. Guo, J. Luan, Q. Wang, J. Lu, S. Shi, and C.T. Liu: *J. Alloy Compd.*, 2014, vol. 584, pp. 530–37.
42. Y.L. Zhao, T. Yang, J.H. Zhu, D. Chen, Y. Yang, A. Hu, C.T. Liu, and J.J. Kai: *Scripta Mater.*, 2018, vol. 148, pp. 51–55.
43. Z. Wang, I. Baker, W. Guo, and J.D. Poplawsky: *Acta Mater.*, 2017, vol. 126, pp. 346–60.
44. D. Liang, C. Zhao, W. Zhu, P. Wei, F. Jiang, Y. Zhang, Q. Sun, and F. Ren: *Mater. Sci. Eng. A*, 2019, vol. 762.
45. S. Yoshida, T. Ikeuchi, T. Bhattacharjee, Y. Bai, A. Shibata, and N. Tsuji: *Acta Mater.*, 2019, vol. 171, pp. 201–15.
46. E.O. Hall: *Proc. Phys. Soc. Sect. B*, 1951, vol. 64, pp. 747–53.
47. G. Liu, G.J. Zhang, F. Jiang, X.D. Ding, Y.J. Sun, J. Sun, and E. Ma: *Nat. Mater.*, 2013, vol. 12, pp. 344–50.
48. V.C. Nardone and K.M. Prewo: *Scripta Mater.*, 1986, vol. 20, pp. 43–48.
49. H. Wen, T.D. Topping, D. Isheim, D.N. Seidman, and E.J. Lav-ernia: *Acta Mater.*, 2013, vol. 61, pp. 2769–82.
50. R.E. Smallman and G.K. Williamson: *Philos. Mag.*, 1956, vol. 1, pp. 34–46.
51. W.H. Hall and G.K. Williamson: *Acta Mater.*, 1953, vol. 1, pp. 22–31.
52. J.Y. He, H. Wang, H.L. Huang, X.D. Xu, M.W. Chen, Y. Wu, X.J. Liu, T.G. Nieh, K. An, and Z.P. Lu: *Acta Mater.*, 2016, vol. 102, pp. 187–96.
53. S. Jahanmir and X. Dong: *J. Tribol.*, 1992, vol. 114, pp. 403–11.
54. Y. Wang and S.M. Hsu: *Wear*, 1996, vol. 195, pp. 90–99.
55. S. Basavarajappa, G. Chandramohan, A. Mahadevan, M. Thangavelu, R. Subramanian, and P. Gopalakrishnan: *Wear*, 2007, vol. 262, pp. 1007–12.
56. X.C. Liu, H.W. Zhang, and K. Lu: *Science*, 2013, vol. 342 (6156), pp. 337–40.
57. X.C. Liu, H.W. Zhang, and K. Lu: *Acta Mater.*, 2015, vol. 96, pp. 24–36.

Publisher's Note Springer Nature remains neutral with regard to jurisdictional claims in published maps and institutional affiliations.